Observations of Intergranular Stress Corrosion Cracking in a Grain Mapped Polycrystal [1]

Non-destructive three dimensional mapping of grain shape, crystallographic orientation and grain boundary geometry by diffraction contrast tomography (DCT) provides opportunities for the study of the interaction between intergranular stress corrosion cracking and microstructure. A stress corrosion crack was grown through a volume of sensitised austenitic stainless steel mapped using DCT and observed in-situ by synchrotron tomography. Several sensitisation resistant crack bridging boundaries were identified, and while having special geometric properties, they are not the twin variant boundaries usually maximised during grain boundary engineering.

Intergranular stress corrosion cracking (IGSCC) is the progressive nucleation and growth of cracks by localized corrosion along the grain boundaries in metals in the presence of stress or strain. Crack growth is driven by the in-elastic deformation at the sharp crack tip. IGSCC is therefore the result of the combination of susceptible material, critical environment and sufficient mechanical driving force. It is a critical failure mechanism in some components of power generation plant (1), where cracking of austenitic stainless steels can result from sensitisation of certain grain boundaries after heat treatment (such as post-weld stress relief) or fast neutron irradiation in a nuclear plant.

---

[1] NOTICE: this is the author's version of a work that was accepted for publication in Science. Changes resulting from the publishing process, such as peer review, editing, corrections, structural formatting, and other quality control mechanisms may not be reflected in this document. Changes may have been made to this work since it was submitted for publication. A definitive version was subsequently published in Science Volume 321, Issue 5887, 18 July 2008, Pages 382-385, DOI: 10.1126/science.1156211

Sensitisation decreases the local resistance of grain boundaries to corrosion. Thermal sensitisation is due to chromium carbide precipitation at the grain boundaries (2). The slow diffusing chromium is depleted in the region adjacent to the carbides, to a degree sufficient to substantially reduce the oxidation resistance. Chromium depletion at grain boundaries also occurs with irradiation damage (3), although point defect creation and changes in dislocation behaviour may also be important factors (4).

Sensitisation resistance is affected by grain boundary structure, which is commonly described using the coincident site lattice (CSL) notation. This describes the orientation relationship between the crystal lattices of grains adjacent to the grain boundary, and is generally obtained using two dimensional electron backscatter diffraction (EBSD) techniques (5). This provides no information on the actual grain boundary plane for most boundaries. The crystallographic habit plane of coherent Σ3 twins is well defined, for example, but not that of incoherent Σ3 twins. However, the grain boundary plane has an important effect on the grain boundary structure (5), and descriptions such as the fraction of Σ3 boundaries in the microstructure neglect this. Nonetheless, this description has been sufficient to enable the resistance to intergranular degradation of materials to be improved by grain boundary engineering (6). This is done typically by maximising the fraction of twin variant grain boundaries ($\Sigma 3^n$, $1 \leq n \leq 3$), or more generally low Σ CSL boundaries ($\leq \Sigma 29$).

High-resolution synchrotron tomography has been applied previously to obtain three-dimensional in-situ observations of intergranular SCC, using sensitised austenitic stainless steel (7). Evidence for crack bridging by individual grain boundaries resistant to cracking was obtained; these non-sensitised, corrosion resistant grain boundaries fail in a ductile manner at high strain. They are proposed to mechanically restrict the opening of the crack tip in a manner analogous to fibres in a composite material. Such crack bridging would reduce the in-elastic crack tip strains in response to the applied stress, and consequently decrease the stress corrosion crack growth rate. Three-dimensional modelling of intergranular stress corrosion crack nucleation, based on these observations, predicts that grain boundary engineering to increase the proportion of sensitisation resistant boundaries significantly increases the incubation period for crack nuclei, and thereby increases intergranular SCC resistance (8, 9). Validation and further development of such IGSCC models, to address intergranular

strains from grain misorientations (10) for example, requires observations of the three-dimensional interaction between cracks and microstructure, and therefore full three-dimensional characterisation of the microstructure itself.

There are a number of approaches to three-dimensional microstructure characterisation. Destructive analysis of the microstructure is possible, although 2D techniques are not generally able to fully characterise a grain boundary. The trace of the intersection between the boundary plane and the surface can be identified, but the inclination of the boundary plane is not known. Thus, only four of the five parameters required for a full grain boundary description can be obtained (5). Statistical 3D boundary descriptions may be obtained from 2D data using stereological methods (11), but they are unsuitable for studies of local events such as crack behavior. Destructive serial-sectioning for 3D characterisation of local features is also possible (see (12) for example). However, such studies are time-consuming, do not necessarily provide data on all grain boundaries, and are difficult to apply to damaged samples that contain cracks. Recently, two non-destructive 3D orientation mapping techniques employing synchrotron radiation have become available, known as differential aperture X-ray microscopy (DAXM) (13) and 3D X-ray diffraction microscopy (3DXRD) (14), respectively. The technique used in this work, called diffraction contrast tomography (DCT), is closely related to 3DXRD and has been developed by some of the authors in collaboration with the Risø group.

DCT currently allows the characterization of plastically non-deformed, polycrystalline materials in terms of 3D grain shapes and crystallographic orientations and provides simultaneously a picture of the material's microstructure using X-ray absorption contrast. Each voxel (15) is assigned to a grain within the characterised volume, and the attenuation as well as the crystal orientation of each voxel is known. The principles and analysis methods of DCT are described in (16, 17), and are briefly summarised together with the use of synchrotron computed tomography (CT) to image the development of the crack in (18). In order to study the interaction of the stress corrosion crack with the microstructure, it is necessary to marry the DCT and CT observations, between which there will be rotational and translational differences.

The sample used was an austenitic stainless steel wire, heat treated to produce a fully recrystallised microstructure, and then thermally sensitised for intergranular SCC.

The sample preparation is described in more detail in (18). The DCT dataset provides a 3D map (Figure 1a) of the grain shapes and their crystal orientations. The map comprises 362 grains, giving some 1600 fully characterised grain boundaries. For visualisation, the grain surfaces are rendered and coloured according to their crystallographic orientation, using the three components of the Rodrigues' vector (24, 25) to obtain RGB values (red/blue/green) with appropriate scaling. The grains' shapes are observed to be self-consistent with their neighbors. The narrow gaps (typically 15-30 μm) between the grains are an artefact of the data processing, and may be removed in a simple post-processing dilation operation. Before this post-processing, the space-filling of the grain map is 59%. The grain boundaries can be described using the relative crystal lattice misorientation between the adjacent grains. This has been done according to the coincident site lattice (CSL) convention, using Brandon's deviation criterion (see e.g. 5). In the 3D grain boundary map (Figure 1b), the low angle boundaries (Σ1), twins (Σ3) and low-Σ CSL boundaries (Σ5 to Σ29) have been highlighted.

After the DCT characterisation, the sample was loaded in a corrosive environment to initiate a stress corrosion crack, the propagation of which was studied in-situ using synchrotron CT (7, 18). Multiple initiation sites were observed, from which a dominant crack coalesced to propagate across the sample. Results presented here are for the final observation before sample failure. A 3D surface rendering of the crack at this stage is shown in Figure 2a. Three holes in this surface can be readily identified. These are regions where the surrounding material is continuous across the crack, and they are therefore ligaments that have been isolated as the crack propagated around them. The sample was then allowed to fail by further stress corrosion cracking, and the final fracture surface, observed by scanning electron microscopy, is shown in Figure 2b. The higher resolution images (inset Figure 2b) at the location of the holes show ductile fracture surfaces, in contrast to the intergranular brittle character of the majority of the surface that is characteristic of IGSCC. The ductile regions are caused by the tearing to failure of the crack bridging ligaments after the final tomography scan. Such regions are distributed over the entire fracture surface, indicating that they also develop during crack growth (7).

A rendering of the fracture surface from Figure 2a is given in Figure 3a, showing its alignment with the 3D grain map. The volume is sectioned at the position of one of the holes, or bridging ligaments, in the intergranular crack. As the DCT and CT datasets are aligned, each facet of the intergranular crack can be associated with a particular grain boundary. Hence the crack can be described in terms of the structure and orientation of the grain boundaries along which it propagates. This combined technique also allows identification of the grain boundary at the position of each of the three holes, or crack bridges, shown in Figure 2a.

An example (crack bridge 1) is shown in Figure 3b, with the trace of the crack on a map of the grain boundaries, coloured according to their CSL designation. The hole in the CT image of the crack coincides with a low angle grain boundary (the misorientation angle between the crystal lattices of the grains is 9.4º±0.05º). The grain boundary normal, obtained by fitting a plane between the grains, was inclined at 19.6º±10º to the tensile stress axis. The uncertainty is largely due to the gaps between the grains in the DCT dataset. Similar analysis shows the hole at crack bridge 2 is located at a Σ11 boundary. Its boundary normal is at 32.2º±10º to the tensile axis. The grain boundary that coincides with the hole at crack bridge 3 is neither a low angle boundary nor a low Σ CSL boundary. It has a crystal misorientation angle of 44.3° and a misorientation axis that is 1.1º±0.05º from <310>. This boundary has strong tilt character, with the misorientation axis lying at 86.8°±10° to the grain boundary normal. The grain boundary plane lies within 3.9°±10º of the {001} pole in one of the two adjoining grains, and within 5.0°±10º of the $\{\bar{1}23\}$ pole in the other, indicating that it has an orientation close to a low {hkl} index plane in both grains. The 10° uncertainty is due to curvature of the grain boundary plane.

Low angle and low-Σ CSL grain boundaries are known to generally have special properties. Similarly, it is proposed that boundaries close to low index planes may be beneficial, despite not being low-Σ CSL (26). Due to the 3D characterisation of the sample we are able to determine the approximate plane of all grain boundaries. The frequency distribution of grain boundary plane orientations obtained from the fracture surface and the bulk microstructure are shown in Figure 4. The bulk microstructure is shown, both including and excluding the Σ3 twins. The number of boundaries on the

fracture surface that are close to low {hkl} index planes, such as {111} is low, when compared to the bulk microstructure.

These in-situ observations are direct confirmation of the resistance of individual grain boundaries to intergranular stress corrosion cracking and their role in crack bridge development. This is consistent with reports that grain boundary engineering to reduce the proportion of sensitised grain boundaries can improve intergranular SCC resistance (5, 6, 9). Furthermore, the results suggest that a specific range of grain boundaries have "special" properties and may be involved in crack bridging during SCC, beyond the twin variant grain boundaries ($\Sigma 3^n$) usually targeted in grain boundary engineering.

Knowledge of the behaviour of individual grain boundaries is most beneficial to the study of intergranular failure. The application of 3D orientation mapping techniques, such as diffraction contrast tomography, may provide local and spatial information on the connectivity and clustering of certain grain boundary structures throughout the bulk material. This more complete description of microstructure, together with understanding of the structure of individual boundaries and their cracking mechanisms, obtained by transmission electron microscopy studies for example (27, 28), is the foundation for more realistic models of crack behaviour. The combined approach described here has potential applications to other forms of degradation including fatigue and transgranular stress corrosion cracking.

References

1. P.M. Scott, *Corrosion* 56, 771 (2000).
2. S.M. Bruemmer, G.S. Was, *J. Nuclear Materials* 216, 348 (1994).
3. P. Scott, , *J. Nuclear Materials* 211, 101 (1994)
4. J.T. Busby, G.S. Was, and E.A. Kenik, Journal of Nuclear Materials, 302, 20 (2002)
5. V. Randle, *Acta Mater.* 46, 1459 (1998).
6. E.M. Lehockey, A.M. Brennenstuhl, I. Thompson, *Corrosion Science* 46, 2383 (2004).

7. L. Babout, T.J. Marrow, D. Engelberg, P.J. Withers, *Materials Science and Technology* 22, 1068 (2006).

8. A.P. Jivkov, N.P.C. Stevens, T.J. Marrow, *Computational Materials Science* 38, 442 (2006).

9. A.P. Jivkov, N.P.C. Stevens, T.J. Marrow, *Theorectical and Applied Fracture Mechanics* 48, 187 (2007).

10. O. Diard, S. Leclercq, G. Rousselier, G. Cailletaud, *Computational Materials Science*, 25, 73, (2002)

11. V Randle, *J Microscopy*, 222, 69 (2006).

12. A.C. Lewis et al, *Materials Science and Engineering A* 418, 11 (2006).

13. B.C. Larson, W. Yang, G.E. Ice, J.D. Budai, J.Z. Tischler, *Nature* 415, 887 (2002).

14. H.F. Poulsen *Three-dimensional X-ray diffraction microscopy. Mapping polycrystals and their dynamics.* Springer Tracts in Modern Physics, Springer, Berlin (2004).

15. A voxel in the 3D dataset is the analog of a pixel in a 2D digital image, such as an EBSD map.

16. W. Ludwig, S. Schmidt, E.M. Lauridsen, H,F. Poulsen, *J. Appl. Cryst*. 41, 302 (2008).

17. G. Johnson, A. King, M.Gonzalves Honnicke, T.J. Marrow and W. Ludwig, *J. Appl. Cryst*. 41, 310 (2008).

18. Materials and methods are available as supporting material on *Science* Online.

19. R. Gordon, R. Bender, G.T. Herman, *J. Theor. Biol*. 29, 471 (1970).

20. A. Koch, C. Raven, P. Spanne, A. Snigirev, *J. Opt. Soc. Am*. A15 (7), 1940 (1998).

21. J.C. Labiche et al, *Rev. Sci. Instr*. 78, 091301 (2007).

22. J. Baruchel et al, *Scripta Materialia* 55, 41 (2006).

23. J.Y. Buffiere, E. Maire, P. Cloetens, G. Lormand, R. Fougeres, *Acta Mater*. 47, 1613 (1999).

24. O. Rodrigues*, J. des Math. Pures. App*., 5, 380 (1840).

25. F.C. Frank, *Metall. Trans*., A19, 3, 403 (1988).

26. V Randle, *Scripta Mater*, 54, 1011 (2006).

27. S.R. Ortner, *Acta Metallurgica et Materialia*, 39, 341, (1991)

28. Y.Z. Huang and J.M. Titchmarsh, *Acta Materialia*, 54, 635, (2006)

29. A. King and G. Johnson wish to acknowledge funding received from the EPSRC (UK). W. Ludwig also acknowledges additional support received from the Danish National Research Foundation.

Figures

Figure 1: Part of the 3D grain map obtained by Diffraction Contrast Tomography (DCT), comprising 169 grains (A total of 362 grains were mapped). The circumference of the sample is outlined, and the plane of the 2D section in Figure 3 is also shown. (a) Grains coloured using a RBG scale according to their crystallographic orientation. (b) Low ∑ CSL grain boundaries coloured (low angle ∑1=orange, ∑3=red, ∑9=blue, other boundaries ∑<=29 purple).

Figure 2: Comparison between computed tomography (CT) and scanning electron microscope (SEM) observation of the IGSCC fracture surface. (a) Surface rendering of CT data for the final crack final step, with three significant bridging ligaments marked. The line marks the plane of the 2D section in Figure 3. (b) SEM image of the fracture surface after failure. Higher resolution SEM observations (Inset) shows ductile features at the positions of the three holes in the CT dataset.

Figure 3: Combined use of DCT and CT data to identify crack bridging grain boundary structure. (a) Crack obtained from CT data is shown in black, at the final step before sample failure, and compared with DCT data of 3D grain shapes. (b) 2D section of the grain boundaries, identified by DCT, compared with the crack path identified by CT. The boundaries are coloured as in Figure 1, and a crack bridge is indicated.

Figure 4: Pole figures showing the frequency distribution of grain boundary planes in the studied sample. {hkl} poles are marked up to {221}. (A) All boundaries, (B) all boundaries excluding S3 twins, and (C) boundaries forming the fracture surface.

Figure S1: Schematic illustration of the formation of extinction and diffraction spots, used to identify grain orientation in DCT.

Figure 1.

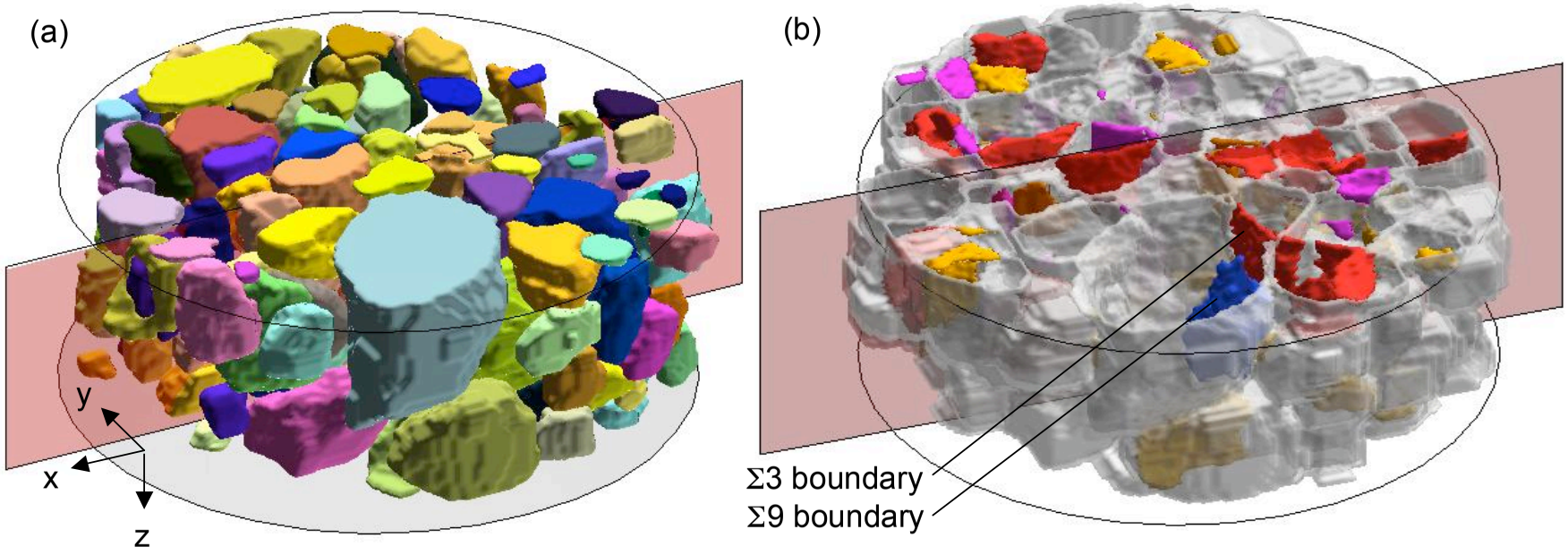

Figure 2.

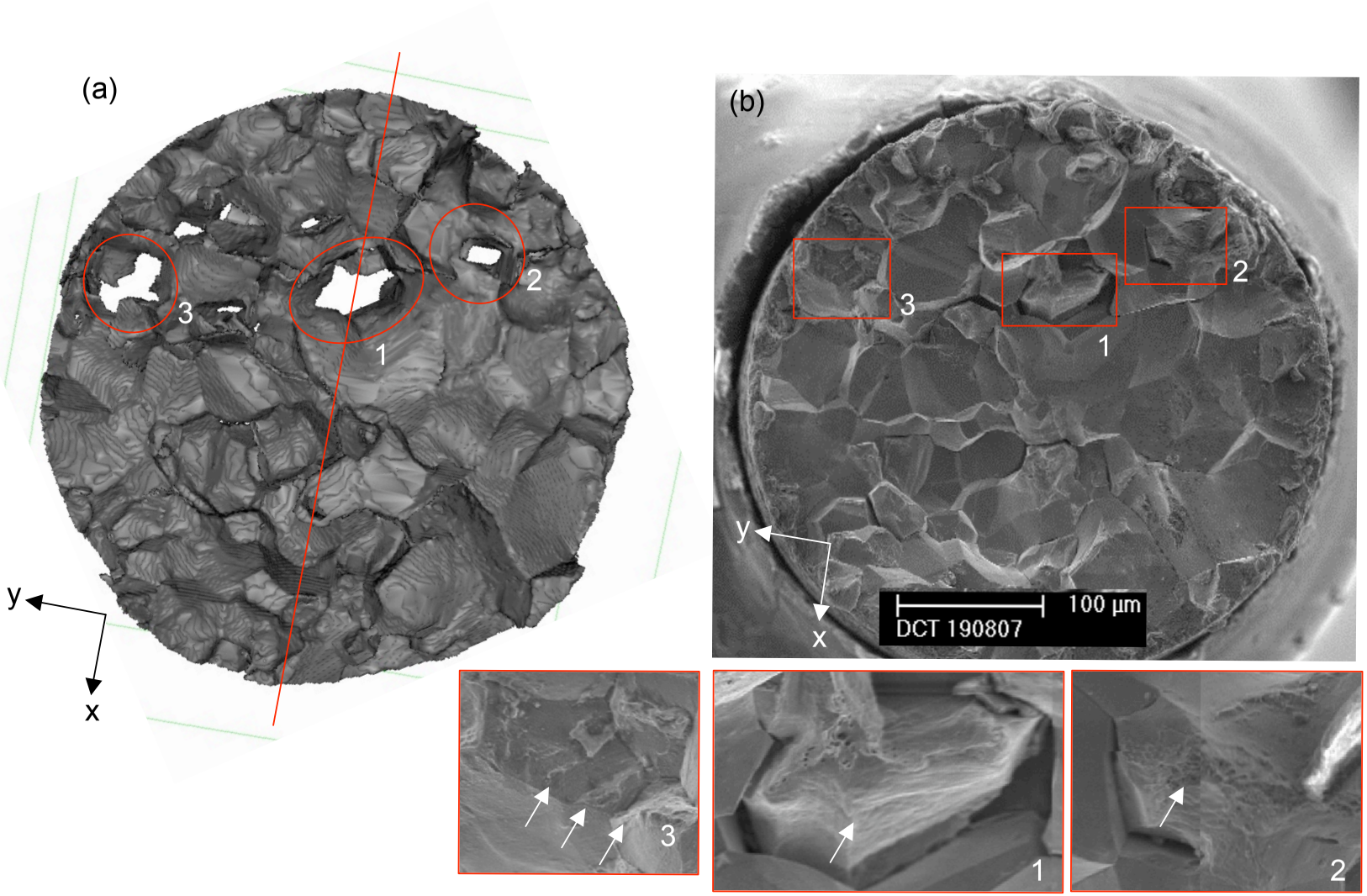

Figure 3.

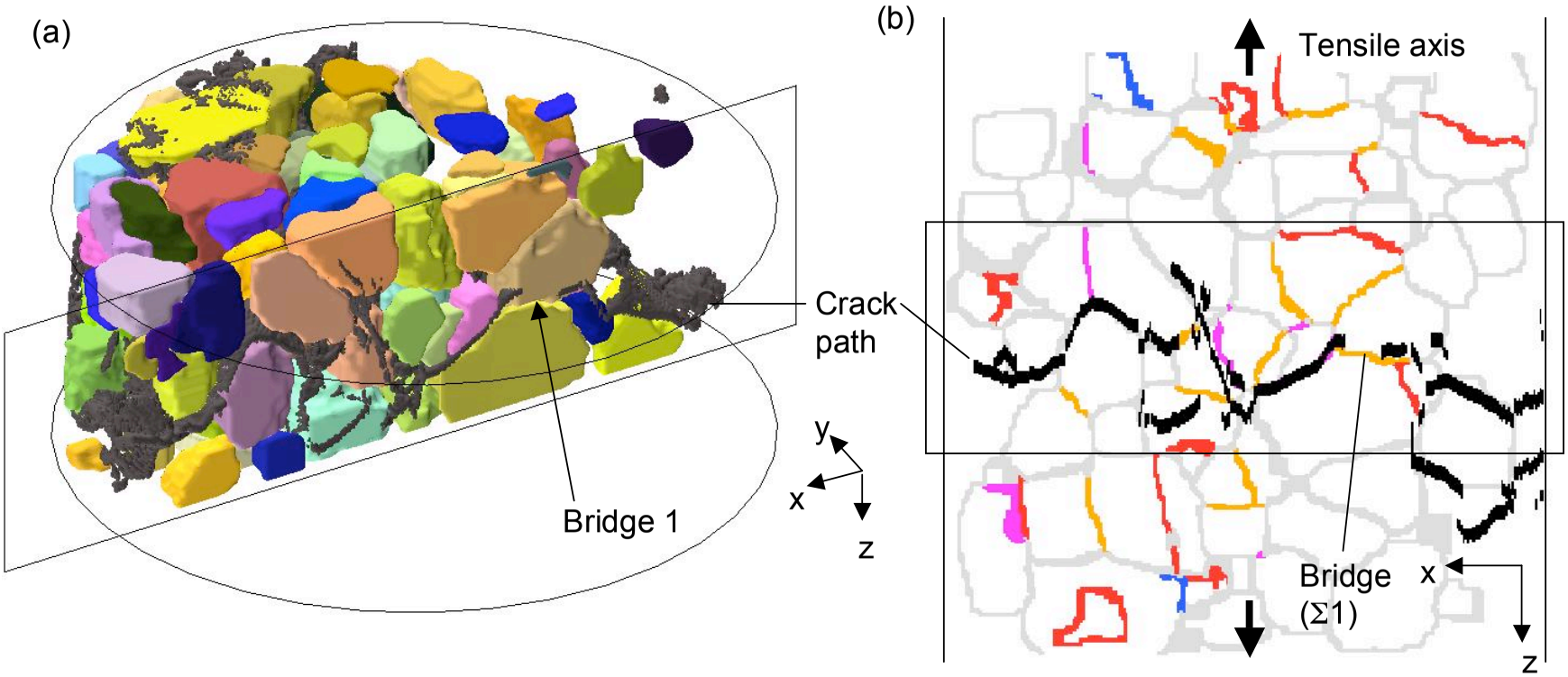

Figure 4.

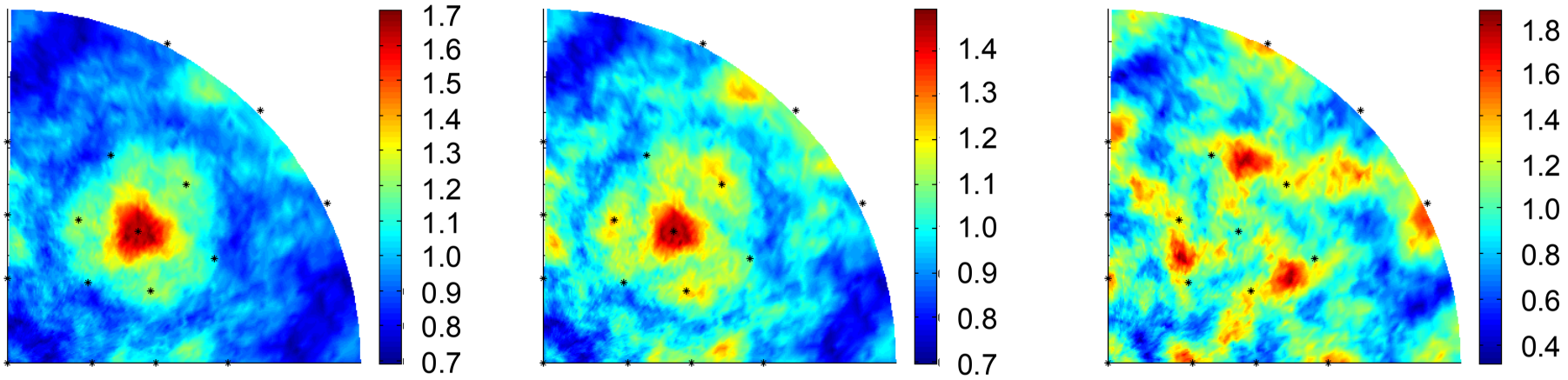

Figure 4. Pole figures showing the frequency distribution of grain boundary planes in the studied same. {hkl} poles are marked up to {221}. (a) All boundaries, (b) all boundaries excluding Σ3 twins, (c) boundaries forming the fracture surface.

Figure 4.

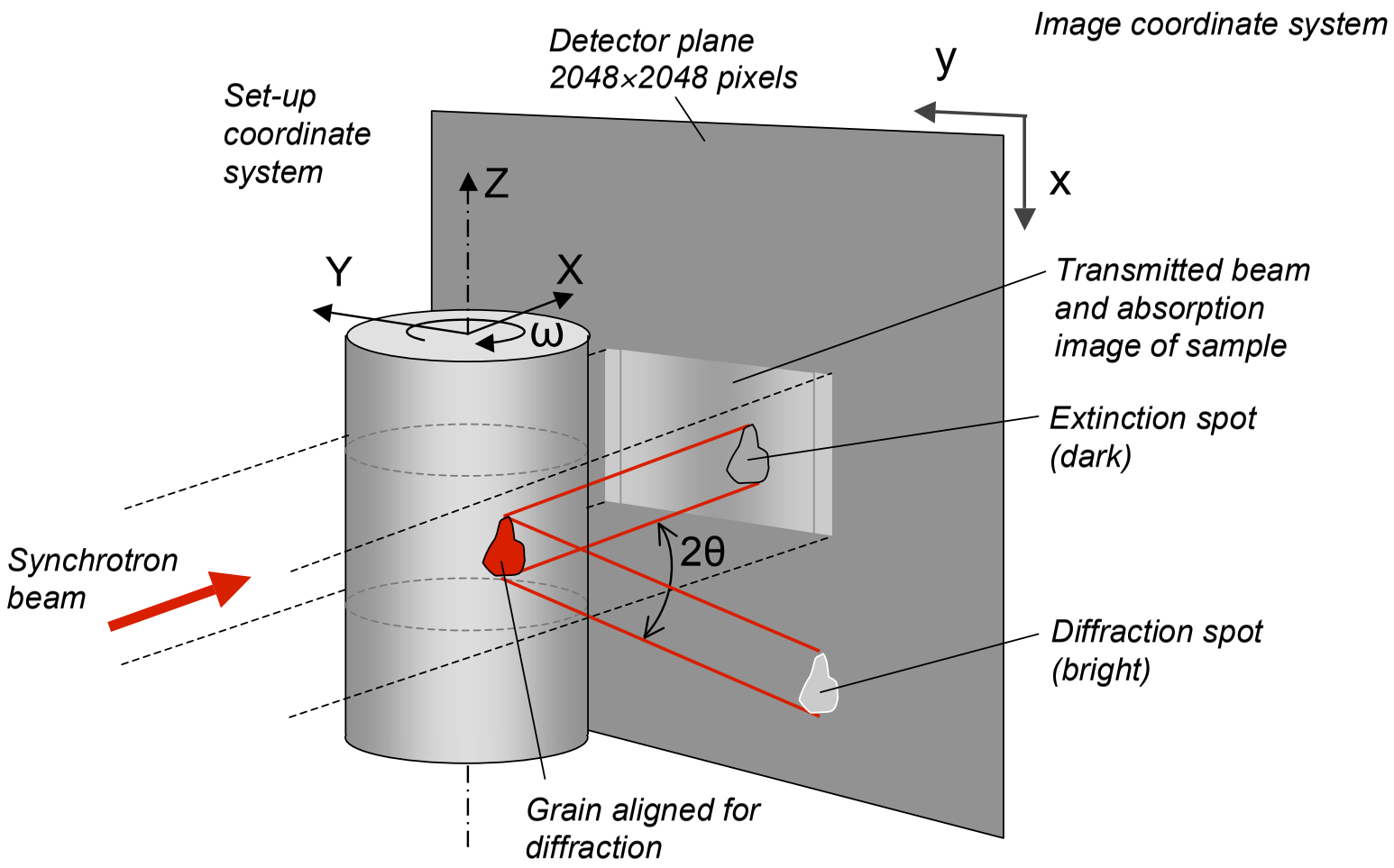
Image coordinate system
Detector plane
2048×2048 pixels
y
x
Set-up
coordinate
system
Z
Y
X
ω
Transmitted beam
and absorption
image of sample
Extinction spot
(dark)
2θ
Synchrotron
beam
Diffraction spot
(bright)
Grain aligned for
diffraction